Experimental Investigation of the Material Removal Rate in Grinding of Calcified Plaque by Rotational Atherectomy

By

Xinxiao Li

A Thesis Submitted to the Faculty of the
Worcester Polytechnic Institute
As a Partial Fulfillment of the Requirements for the
Degree of Master of Science
in
Mechanical Engineering

Committee members:

Professor Yihao Zheng
Professor Yuxiang Liu
Doctor Christopher Nycz

ACKNOWLEDGEMENTS

I am grateful for the countless support provided by many people along the way to my degree.

First, I would like to express my gratitude to Professor Yihao Zheng for his outstanding guidance and support that made this thesis project possible. I have learned from him in many aspects: technical writing, conducting research and giving the presentation. He taught me to be diligent, and he is the most hardworking and wise man I have ever known. He has been inspiring me to always carry passion and perseverance with me. I also would like to express my appreciation to the committee members: Professor Yuxiang Liu and Doctor Christopher Nyzc, thank you for your time and your guidance on my thesis.

I also would like to express my gratitude to my co-workers in Professor Yihao Zheng's group. I am incredibly grateful to Ms. Katerina Angjeli and Mr. Patrick Chernjavsky. They helped me a lot during the research and provided me with some valuable suggestions. I want to express my gratitude to Sara A. Frunzi. She helped me to process the plaster samples and helped with the experiment. I would also like to express my appreciation for the time and support I received from the Mechanical Engineering department. I am incredibly thankful for Ms. Barbara Furman. She has always been accommodating and patient with my purchasing orders.

I am thankful to my parents for their motivations and support; they gave me a chance to study at WPI. WPI funded my studies, and I am thankful for their support.

We acknowledge the facility support from PracticePoint and Lab for Education and Application Prototypes (LEAP) at Worcester Polytechnic Institute (WPI). This study is supported by the freshman research program within WPI Mechanical Engineering and the Early Research Experience in E Term (EREE) program at WPI

TABLE OF CONTENTS

LIST OF TABLES

LIST OF FIGURES

ABSTRACT

Rotational atherectomy (RA) is a minimally invasive interventional procedure to remove the calcified atherosclerotic plaque from arteries, restore blood flow, and treat cardiovascular diseases. It uses a high-speed, metal-bonded diamond abrasive grinding wheel to pulverize the calcified plaque into absorbable debris via a catheter through the artery. The grinding wheel is driven by a long flexible shaft rotational up to 230,000 rpm. RA procedure has complications including peri-procedural myocardial infarction, stroke, vascular access complications, coronary dissection, abrupt vessel closure, and perforation. RA operational guidelines, including the grinding wheel size and rotational speed, have been investigated to lower complication rates. However, the guidelines are still lacking consensus, and there is confusion in the grinding mechanism of RA. Specifically, the material removing rate (MRR) of RA under different wheel sizes and rotational speeds is unclear.

This study aims to investigate RA MRR over a range of grinding wheel sizes and rotational speeds based on a tissue-mimicking phantom. Three grinding wheel sizes, 1.25, 1.5, and 1.75 mm in diameter, and three-wheel rotational speeds, 120,000, 150,000, and 180,000 rpm, were investigated. A tissue phantom was 3D printed to simulate the diseased region of the artery with calcified atherosclerotic plaque. The surrogate for the calcified plague was made of gypsum plaster and inserted inside the tissue phantom. The MRR was presented as the luminal area gain and measured by microscopy and image processing.

The increase of either the grinding wheel size or rotational speed leads to a higher MRR and luminal gain in RA. The highest MRR and luminal gain achieved in this study by a 1.75 mm diameter grinding wheel rotational at 180,000 rpm were 2.49 mm^2/ three pass and 5.08 mm^2,

respectively. And the lowest MRR and luminal gain produced by the 1.25 mm diameter grinding wheel rotational at 120,000 rpm were 0.59 mm^2/pass and 1.22 mm^2, respectively. During RA with the same grinding wheel at a constant rotational speed, with the increase of the number of grinding passes, the MRR decreases. This study provides a thorough understanding of the wheel size and speed effects on RA MRR and engineering insights for potential improvements in RA devices and clinical operational guidelines.

Keywords: Material removal rate (MRR), Rotational speed, Rotational atherectomy, Calcified plaque grinding, Grinding wheel size, Tissue Phantom

CHAPTER 1

INTRODUCTION

1.1 Atherosclerosis

Cardiovascular disease (CVD) is the leading cause of morbidity and mortality, with 62 million patients in the US [1, 2]. In 2017, 868,622 people died because of CVD in the US [3], and approximately 18.6 million people died due to CVD in 2019 globally [2, 3]. CVD leads to expenses on clinical treatment. Between 2016 and 2017, the total cost of CVD was $363.4 billion [3]. Atherosclerosis is the leading cause of CVD, including coronary artery and peripheral arterial diseases [4]. It thickens the arterial wall with the accumulation of fatty and calcium materials (also known as plaque), narrows the arterial lumen, and decreases blood flow into downstream tissues, depriving nutrition and oxygen for proper functions. Figure 1.1 presents the development of atherosclerotic plaque. Atherosclerosis begins with an increasing level of the circulating lipid in the bloodstream and the accumulations of foam cells in the intimal layer of the artery [5]. Then the necrotic core inflames in the walls of arteries and leads to fatty streaks. The fatty streaks and the fibrous plaque build continuously as the fibrous plaque grows on fatty streaks [6]. Next the tissue inside the fibrous cap calcifies and causes hardening and narrowing of the artery.

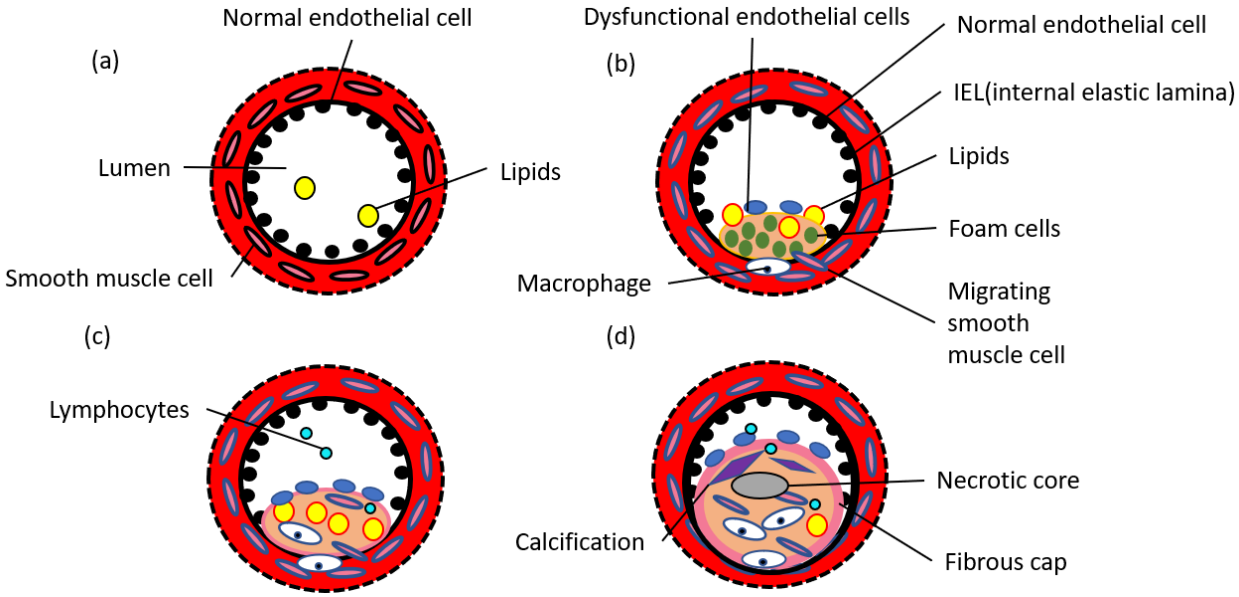

Figure 1.1 Progression of atherosclerotic plaque. (a) The normal vessel, which has the normal level of circulating lipid. (b) The fatty streak and lipid accumulated in the intima, macrophages engulf lipid and become foam cells. (c) The lipid, macrophages, and smooth muscle cells continued to accumulate, with other immune cells such as lymphocytes will be trapped in the fibrous cap. (d) The graph shows a stable fibro atheromatous plaque, the mixture of lipid, smooth muscle cells, necrotic core and the calcification of the tissue are separated by the fibrous cap from the lumen [7] (the original graph is from Cellular and Molecular Pathobiology of Cardiovascular Disease).

1.2 Treatments of Atherosclerosis and Atherectomy

Atherosclerosis can be treated by applying medications and angioplasty. Medications such as statins and other cholesterol medications can effectively prohibit atherosclerosis from becoming progressively worse [8], but they cannot remove the pre-existing lesions, especially the hardened calcified lesion. For those complex lesion cases, percutaneous coronary intervention (PCI) can be applied to remove the calcified lesion and open the blocked artery [9].

Angioplasty is a procedure used to extend the narrowed coronary arteries in the heart [10], as shown in Figure 1.2 The whole process involves coronary angioplasty and stenting. A

guidewire will be threaded through the diseased location once the obstructions is located. A balloon catheter will be placed at the center of the diseased area and inflated to widen the clogged artery [11]. A stent is expanded with the balloon dilation through the artery and implanted permanently at the diseased section to keep the artery open [11]. The atherosclerotic plaque is soft in the early stages, and angioplasty procedures can open narrowed arteries. However, with the development of atherosclerosis, the wall of the artery thickens, and fatty deposit inside the vessel wall is calcified and hardened. Eventually, the hardness of the calcified plaque will be similar to bone [12]. Treating those cases simply with the balloon and sent deployment can lead to severe complications because of the high pressure needs to defeat the stiff calcified lesions [13]. In this case, it is necessary to use the rotational atherectomy (RA) procedure to remove the calcified material and restore part of the elasticity of the lesion.

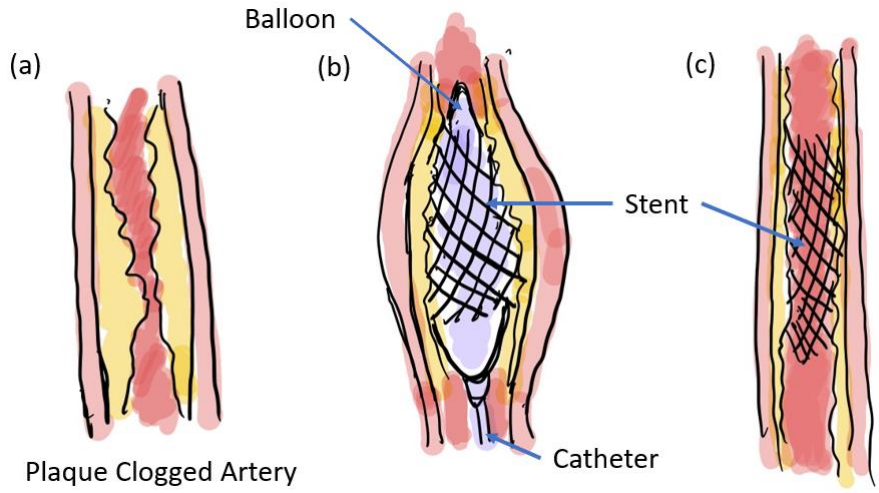

Figure 1.2 Procedure of angioplasty. (a) The diseased artery with calcified lesion. (b) The balloon is inserted in the artery and inflated to expand the stent and narrowed artery wall. (c) The stent is implanted at the diseased section.

RA is an interventional procedure that is used for plaque ablation by a high-speed rotational, metal-bonded, diamond-abrasive grinding wheel driven by a flexible drive shaft [14]. As shown in Figure 1.3, a stainless-steel guidewire leads the wheel to move translationally, and a flexible coil shaft drives the wheel to rotate about the guidewire. The rotational shaft is contained within a stationary plastic sheath with saline flows through the sheath for lubrication and cooling. This device is most effective in removing complex inelastic lesions [15].

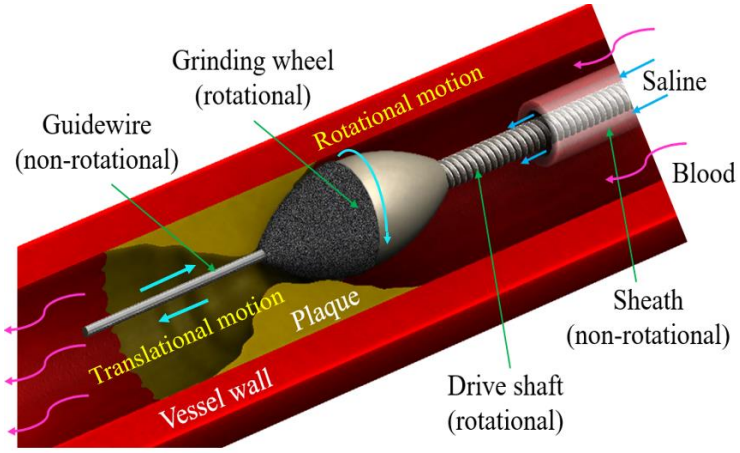

Figure 1.3 Rotational atherectomy procedure.

RA was invented in 1988 for calcified lesions treatment [16]. With the development of alternative methods and due to its technique's complexity, the uses of RA decreased for a while [16]. However, the number of medical treatments performed by RA has increased in recent years due to the increasing application of drug-eluting stents and the aggressive treatment of longer lesions [16].

RA has been troubled with several complications [16], including restenosis (the regrowth of plaque after removal), vessel dissection and perforation (relates to excessive grinding), and slow-flow or no-reflow (potentially caused by large debris blocking downstream capillaries). Table 1 shows the main RA complications types and rates.

Table 1.1: Major complications and rates of RA [51, 52]

RA Complications	Rates
Myocardial infarction	1.2-1.3%
Emergency CABG	1-2.5%
Artery dissection	10-13%
Abrupt vessel closure	1.8-11.2%
Slow-flow phenomenon	1.2-7.6%
Perforation	0.4-2%
Severe spasm	**1.6-6.6%**

Associated with these complications is the lack of a consensus in RA operational techniques including the grinding wheel rotational speed and size selection. For example:

Grinding wheel size selection:

- Tomey indicates the max burr to artery (B/A) ratio (the ratio of the burr diameter to the artery inner diameter) is 0.5 to 0.6 [17].
- Sharma indicates the maximum B/A ratio is 0.4 to 0.6 [18].

- P.L. Whitlow [18] and R.D. Safian [19] suggest the B/A ratio should be of 0.7.

RA rotational speed:

- Tomey suggests the rotational speed of RA should between 140000 to 150000 rpm [17].
- Experts in Europe recommend 135000 to 180000 rpm as the optimal range of wheel rotational speed [20].
- Paula Mota indicates the lower rotational speed of 130000 to 160000 rpm can ensure both the success rate and the safety of the RA procedure [21].

Several engineering studies have been conducted on RA to understand its grinding mechanism including grinding force [22-25], temperature [26-28], debris size [29], wheel motion [30-32], wheel design [33-35], and abrasive cutting mechanics [36]. However, the plaque material removal rate (MRR) in RA still lacks investigation. A clinical study evaluated the effect of low (120,000 rpm) or high (220,000 rpm) grinding wheel rotational speed effect on the RA MRR, but was not able to obtain a conclusive result [37]. Another study also investigated two grinding wheel speeds (110,000 and 190,000 rpm) via both engineering bench-top setup and in vivo human subjects and found low-speed RA could achieve a higher MRR [38]. These two studies demonstrated the clinical interest in RA MRR, but were not sufficient to provide a thorough understanding of the wheel rotational speed effect on the RA MRR, due to the limited number of speeds under evaluation.

1.3 Study Goal and Objectives

The goal of this study is to understand the grinding wheel rotational speed and wheel size effect on RA MMR. To achieve this goal, three research objectives are listed as following:

1) Establish setup and experimental method for MRR investigation.
2) Understand the grinding wheel rotational speed effect on RA MRR.
3) Understand the grinding wheel size effect on RA MRR.

In this study, a tissue phantom was designed and used as the calcified plaque surrogate, and RA was performed. Three different grinding wheels (1.25, 1.5, and 1.75 mm in diameter) were tested under three different rotational speeds (120,000, 150,000, and 180,000 rpm). The MRR was presented as the change of the luminal area per three passes. The plaque surrogate specimen was characterized by microscopy and image processing. The detailed experimental setup and methodology are introduced in Chapter 2; the results are presented in Chapter 3; an RA MRR model analytically derived is discussed in Chapter 4; the conclusions and future study are presented in Chapter 5.

CHAPTER 2

EXPERIMENTAL SETUP AND METHODS

2.1 Experimental Setup

The Rotablator™ Rotational Atherectomy System (Boston Scientific, MA) was used in this study. As shown in Figure 2.1, the RA grinding wheel, via a flexible shaft, was driven by an air turbine. The wheel rotational speed was controlled by a pressure regulator that can adjust the compressed air pressure applied to the air turbine. The translation of the grinding wheel was controlled by a motorized linear stage. The grinding wheel, at the tip of the catheter, was introduced through a 3 mm inner diameter sheath into a PVC tube, simulating the femoral access. The PVC tube, as part of the arterial simulator, had blood-mimicking water pumped through at a rate of 30 mL/min, to simulate the blood flow in the coronary artery [32]. The PVC tubes were connected to the tissue phantom which simulated a diseased narrowed coronary artery with calcified plaque.

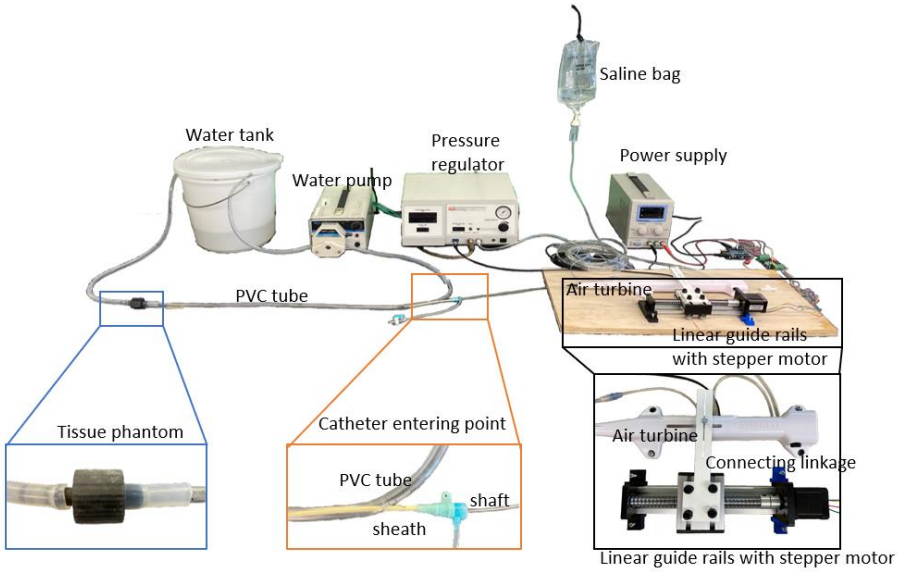

Figure 2.1 Experimental setup.

The sizes of the grinding wheel applied in this study were 1.25, 1.5, and 1.75 mm. During the test, the grinding wheel moved translationally through the calcified plaque surrogate within the tissue phantom at a speed of 1 cm/s back and forth, as shown in Figure 2.2.

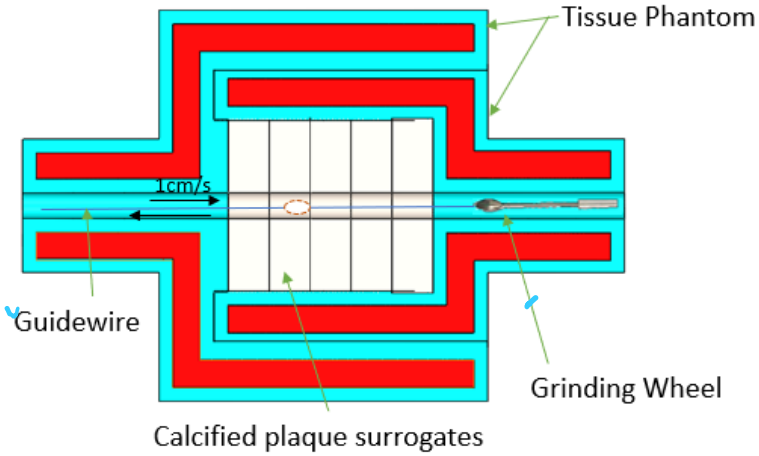

Figure 2.2 Grinding wheel moves translationally through the tissue phantom.

2.2 Tissue Phantom

The tissue phantom, as designed in Figure 2.3, was printed by Connex3 Object 260 multi-material 3D printer. It consists of two different materials. Polypropylene material (marked in red) served as the base structure to support the phantom. The rubber material marked in blue (Tango Black Plus, Stratasys), which has the similar tensile strength as coronary artery wall according to previous studies from Garcia-Herrera and Claes [52, 53], was coated on the polymer base to simulate the soft arterial wall. The rubber helped to seal the tissue phantom and prevent leakage. When testing, the plaster stacks were inserted into the tissue phantom, and the two parts of the

phantom were pressed together ensure the gapless contact among the plaster disks. The plaster disks served as the calcified plaque surrogate and have the thickness of 3 mm. The inner and outer diameter of the plaster disk were 2 mm and 12.8 mm, respectively. Five plaster disks were stacked together with the inner holes aligned with the 3D-printed rubber-coated channel and placed inside the tissue phantom. When testing, the grinding wheel moved translationally through this aligned channel with the speed of 1 cm/s back and forth; after grinding, eight surfaces of the five disks were examined under the microscope to qualify the cross-sectional area change. The two surfaces on the end of the plaster stacks were excluded from the examination for contacting the rubber surfaces. This device allowed us to simulate the diseased artery with calcified lesion and made it easy to measure the lumen diameter.

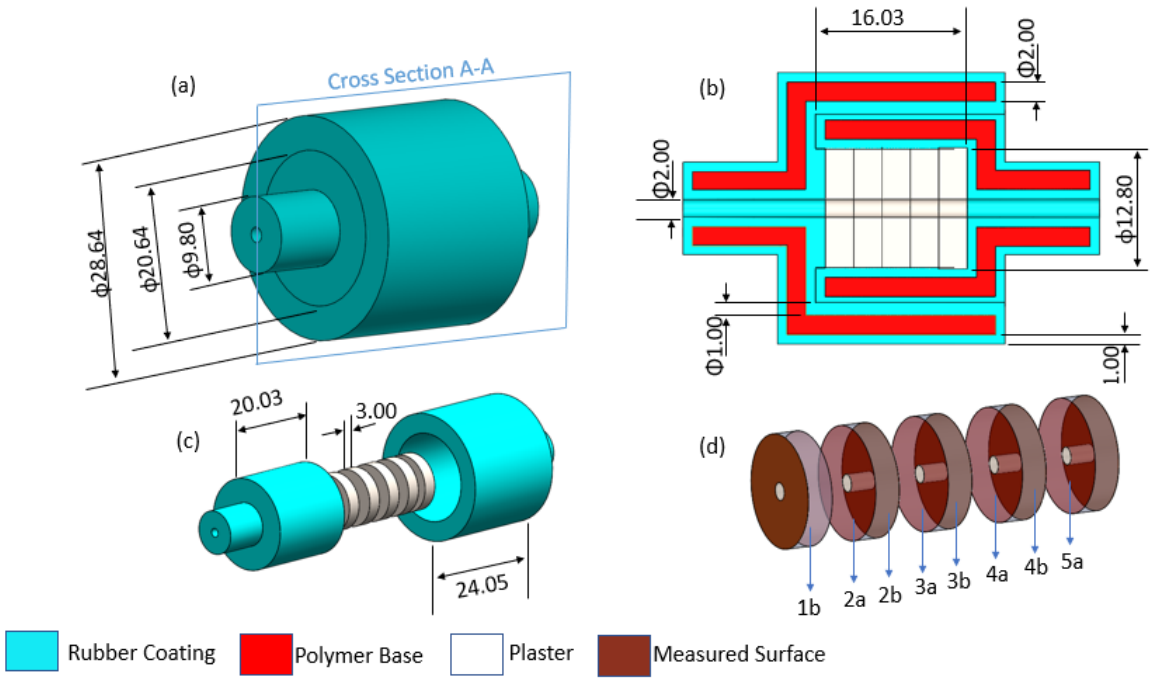

Figure 2.3 Tissue phantom design with (a) overall and (b) inner dimensions (unit: millimeter) and materials, and (c) assembly with graphite plaque surrogate with (d) surfaces for microscopic characterization for MRR marked in red.

2.3 Calcified Plaque Surrogate

Different calcified plaque surrogates have been applied in the previous studies for benchtop tests. For example, Raiders [39] and Tzafriri [40] used the plaque specimens harvested from cadavers in their experiment to investigate the treatment efficacy; Robert S [41] utilized the human ex-vivo calcified plaque to evaluate the efficacy of a percutaneous treatment; Kawase [42] used different sizes of calcium tubes that were made of calcium sulfate dehydrate to test the effectiveness of the scoring balloon catheter in expanding. Riel used plaster tubes with different thicknesses as models to test the efficacy of a scoring balloon catheter and a conventional balloon catheter.

Currently, there is no commonly accepted engineering or animal model to replace the calcified plaque. For engineering benchtop tests, both inorganic and biological materials have been used as calcified plaque surrogates in the previous studies. Those materials are listed as below:

- Biological materials for calcified plaque surrogate include bovine bone [43], CPL800 AND CPL 1000 series [44].
- Inorganic calcified plaque surrogates include plaster [45], cement [46], calcium tube [42], mixture of plaster and animal tissues [47], and graphite.

Ultracal-30, as a plaster material, has been proven to be effective in simulating calcified plaque. Several studies have suggested that the plaster made by Ultracal-30 is a suitable material that can be used as the replacement of human calcified plaque. Scott's study investigated this

topic. In his experiment, various materials were evaluated for the composition compared to human calcified plaque, including plaster, cement, plaster mixed with porcine blood, cement mixed with gelatin, cement mixed with porcine blood, and plasma [47]. A mostly rigid and visibly calcified human plaque was used as the reference standard when measuring the hardness of those materials. Penetration speed test was used to determine the hardness of the material. Among all those five materials, only plaster satisfied toughness, ease of preparation, and catheter damage evaluation standards. This indicates that the bare plaster has similar mechanical properties as human cadaver calcified plaque [47]. Besides, Robert S. identified the plaster (made by Ultracal-30) as an analog that has comparable mechanical properties (hardness, stiffness, and density) to femoral artery calcified plaque samples [48].

Mold casting is commonly used to fabricate calcified plaque surrogates from Ultracal-30. In this study, as shown in Figure 2.4, a three-steps procedure based on 3D printing has been developed to fabricate the calcified plaque surrogate specimen that were previously introduced in Figure 2.4 (d).

Step 1: Flexible silicone mold (FSM) design and fabrication

Considering the brittleness of the plaster and the specimen geometry as a thin disk (Figure 2.3 (d)), an FSM was developed to facilitate the demolding. The FSM was designed to fabricate eight specimens in one batch, as shown in Figure. 2.4 (a) (CAD model using the same blue color to introduce the design). Steel rods can be inserted into the wells to create channels for simulating the arterial lumen.

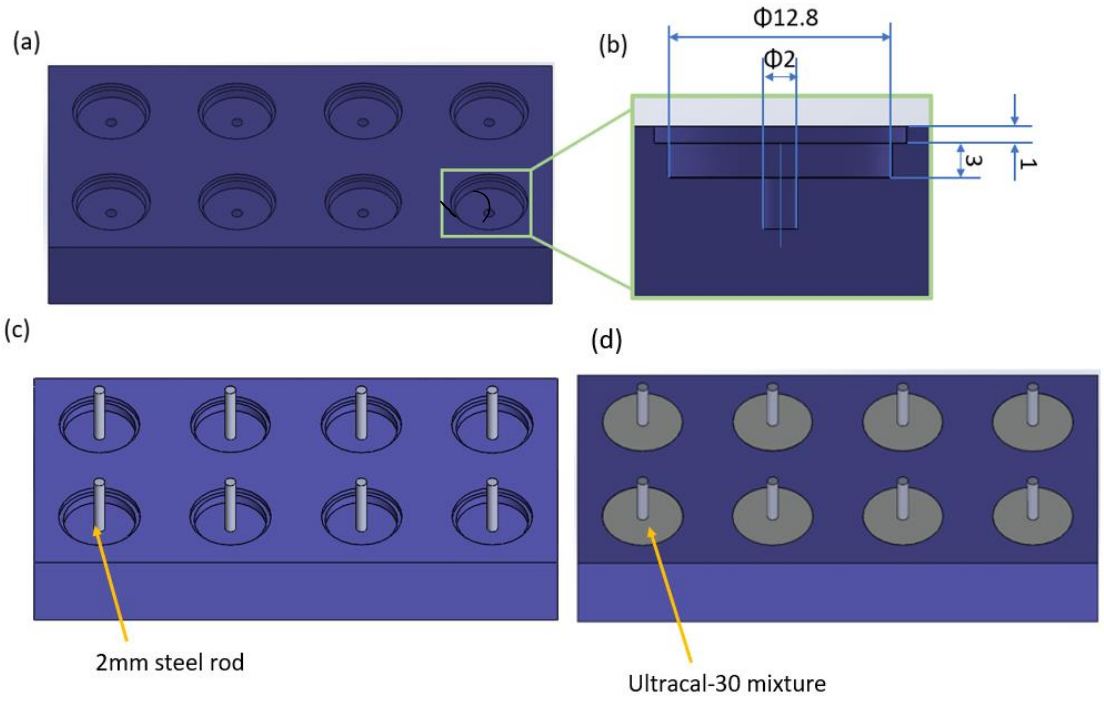

Figure 2.4 Procedure of modeling calcified plaque surrogates: (a) FSM. (b)Transection of a hole on silicone mold. (c) Insert ϕ2 mm rods into the holes on silicone mold. (d) Pour the Ultracal-30 mixture into the silicone mold.

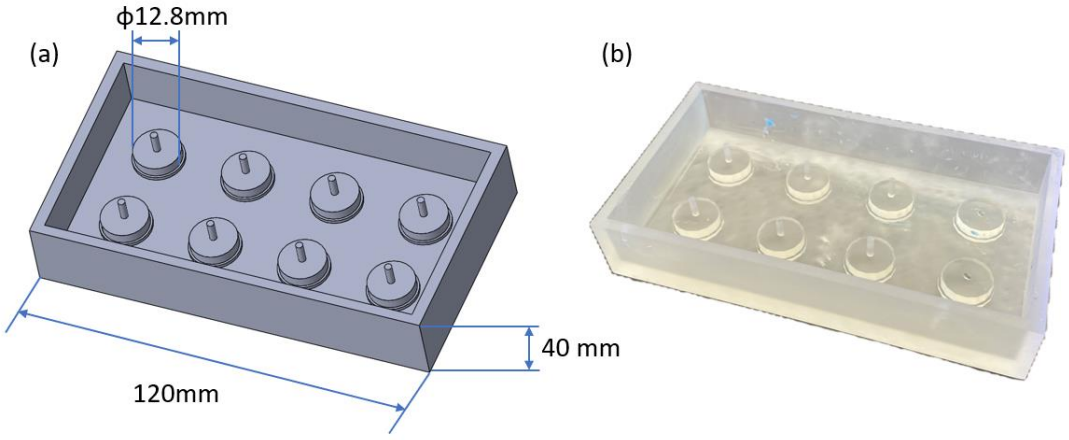

Figure 2.5 Rigid mold for FSM: (a) CAD and (b) 3D printed part by Object 260.

To mold silicone for FSM fabrication, a rigid mold was 3D printed by Object 260 (Stratasys, MN), as shown in Figure 2.5 (b). Before silicone molding, a coating (Smooth-On, Universal Mold Release) to facilitate demolding was applied on the inner surface of the rigid mold. Mold Star 30 (produced by SMOOTH-ON) was selected for silicone modeling. Solutions A and B were mixed in the volume ratio of 1:1 and poured into the rigid mold, cured for 2 hours in the pressure pot at 60 psi. The FSM is shown in Figure (2.4 (a)). Steel rods of 2 mm diameter were inserted into the FSM, as shown in Figure (2.4 (c)), to create the lumen.

Step 2: Ultracal-30 casting in FSM

The Ultracal-30 powder, mixed with water in a weight ratio of 38:100. The Ultracal-30 mixture was poured into the FSM. The FSM with Ultracal-30 mixture was placed inside a pressure pot (2.64 Gallon (10 Liters), TCP Global Commercial) at 60 psi pressure for 1 hour to collapse the bubbles for uniform and consistent specimen properties.

Step: 3: Post processing of the specimen

The casted specimens were removed from the FSM and the steel rods were punctured out to form the lumen. The casted specimens were then inserted into a specimen finishing fixture (SFF) to clean the casting flash and gain accuracy in thickness. The SFF design is shown in Figure 2.6 (a), and 3D printed by Object 260, with PVC material. When inserted, the casted specimen has extra 2 mm thickness on the top for abrasive polishing. Sandpaper was used to polish the top surface of specimen. This post-processing process is shown in Figures 2.6 (a) and (b).

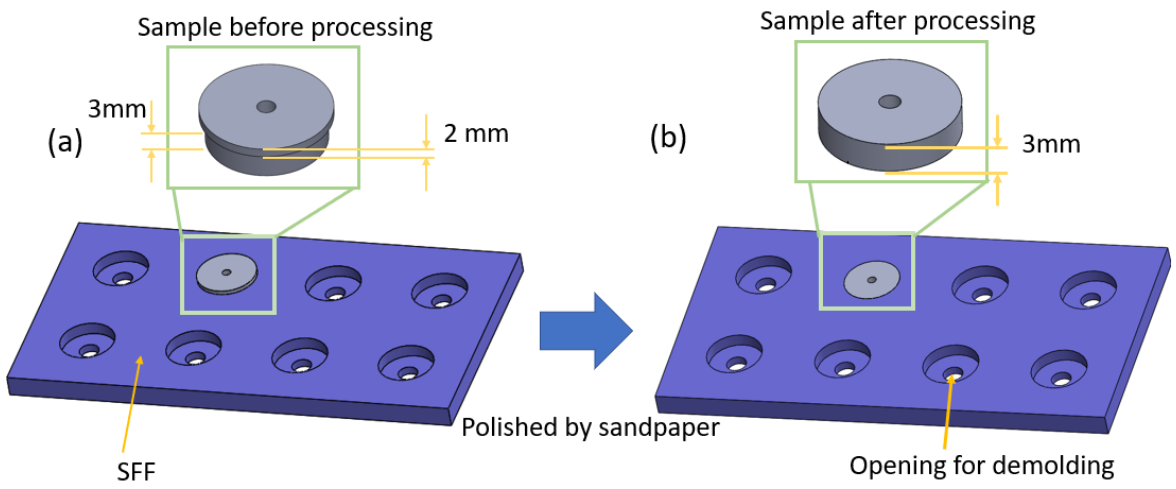

Figure 2.6 The main post processing process for calcified plaque surrogate: (a) Insert the specimen in to SFF. (b) Polish the surface by using sandpaper and remove the 2 mm thick edge on the top of specimen.

2.4 Experimental Design

We investigated the RA MRR under three grinding wheel rotational speeds in this experiment: 120,000, 150,000, and 180,000 rpm. Three sizes of grinding wheels (1.25, 1.5, and 1.75 mm in diameter) were tested. The cross-section area of the plaster specimen lumen on the eight surfaces was measured in every three passes. The mean and standard deviation of the cross-sectional luminal gain and MRR for eight surfaces (1b,2a,2b,3a,3b,4a,4b,5a, shown in Figure 2.3 (d)) were calculated. Each trial was tested for three times to ensure the repeatability of the experiment.

2.5 MRR Measurement via Image Processing

The specimens' luminal gains after RA grinding were measured by a microscope, the magnification during imaging was maintained constant across specimens, enabled by the same

thickness (As show in Figure 2.6 (a)). A series images of the specimen cross-sectional area with the increasing grinding passes is shown in Figure 2.6 (b). At the same magnification, and at the same height of the specimen, a ruler was imaged for pixel size calibration.

The image processing software ImageJ (version 1.52a) developed by the National Institute of Health) was applied in this project to measure the luminal area of each cross-sectional surface. For each rotational speed 120,000, 150,000, and 180,000 rpm, after every three passes of grinding, the eight surfaces mentioned above (Figure 2.6 (d)) were measured under a microscope for cross-sectional area quantification. As shown in Figure 2.7 (a), the lumen can be identified as the darker region on the microscopic image.

To identify the luminal region, thresholding was adjusted to 13.86%. The number of pixels in the luminal area were calculated. The pixel size was calibrated with the ruler image to be 360 pixels/mm. Figure 2.7 (b) shows an example series of microscopic images, demonstrating the luminal gain over 15 grinding passes at an interval of 3 passes at the grinding wheel speed of 180,000 rpm.

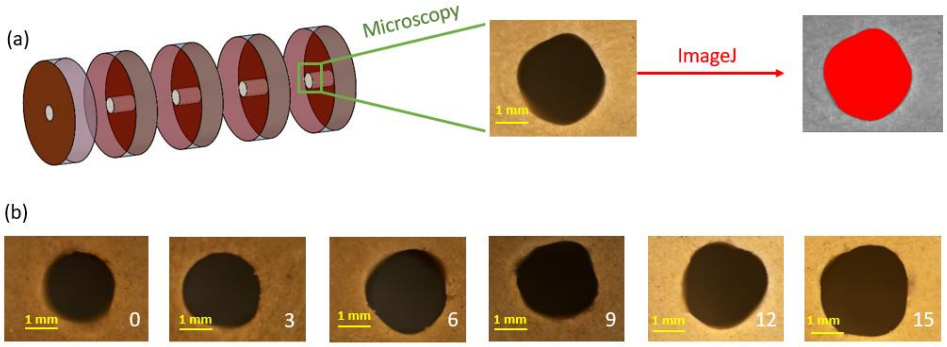

Figure 2.7 Image processing of (a) a microscopic imaging of the cross-section lumen on the plaster specimen and luminal pixel thresholding imageJ and (b) the cross-sectional area increase over 15 passes at a rotational speed of 180,000 rpm.

To quantify the RA MRR, we considered measuring the change of the cross-sectional luminal area an optimal method, comparing to the mass change characterization for the following reasons:

1. The plaster is a porous material that can absorb water, which is going to complicate the measurement.
2. Direct measure of the lumen diameter using calipers is challenging because oftentimes the ground lumen turned out to be non-circular due to the gravity effect of the grinding wheel and the bending of the guidewire.

CHAPTER 3

RESULTS

Figure 3.1 shows the luminal gain after 15 passes of grinding at different grinding wheel sizes and rotational speeds. The black dashes on top of each bar are the standard deviation of the data. At the rotational speed of 120,000 rpm, the luminal gains of the samples corresponding to the grinding wheel sizes 1.25, 1.5, and 1.75 mm are 1.22, 2.22, and 3.64 mm^2. The corresponding area changes at the rotational speeds of 150,000 rpm are 2.25, 2.73, and 4.48 mm^2. The luminal gain at 180,000 rpm of different grinding wheels sizes are 3.14, 3.57, and 5.09 mm^2. The detailed results on luminal gain at different grinding wheel rotational speeds and sizes are summarized in Table 3.1. An analysis of variance (ANOVA) model of one group of test result was calculated to indicate that the grinding wheel speeds and sizes do control the RA MRR, as shown in Table 3.1.

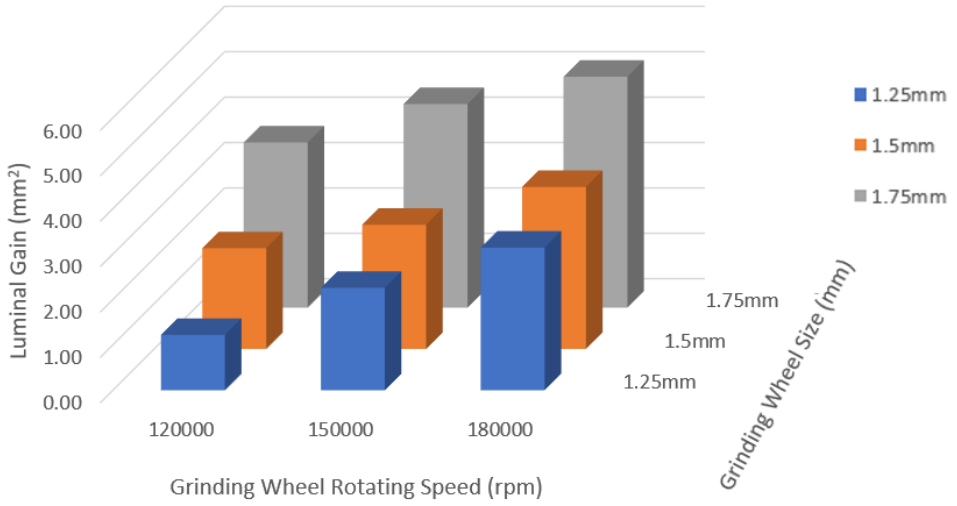

Figure 3.1 Luminal gain of samples at different grinding wheel sizes and rotational speeds.

Table 3.1 Luminal gain at different grinding wheel rotational speeds and sizes after 15 passes of RA

		Grinding wheel diameter [mm]		
		1.25	1.5	1.75
Grinding wheel rotational speed [rpm]	120,000	1.22 ± 0.013	2.26 ±0.012	3.14 ± 0.009
	150,000	2.22 ± 0.011	2.74 ± 0.009	3.57 ± 0.011
	180,000	3.64 ±0.013	4.48 ±0.011	5.09 ±0.010

The uncertainties above may come from the bending of the guidewire, bouncing of the grind wheel, specimen defects, and the thresholding of the image processing.

Table 3.2 Two-factor ANOVA model of MRR at different grinding wheel speeds and sizes for one group of test result

Anova: Two-Factor Without Replication

SUMMARY	*Count*	*Sum*	*Average*	*Variance*
120000 rpm	3	2.47684	0.825613	0.289002
180000 rpm	3	7.00723	2.335743	0.064446
150000 rpm	3	5.31548	1.771827	0.147905
1.5mm	3	4.64217	1.54739	1.05252
1.25mm	3	4.04738	1.349127	0.528251
1.8mm	3	6.11	2.036667	0.291783

ANOVA

Source of Variation	*SS*	*df*	*MS*	*F*	*P-value*	*F crit*
Speeds	3.493814	2	1.746907	27.80651	0.004502	6.944272
Wheel sizes	0.751411	2	0.375706	5.980318	0.062809	6.944272
Error	0.251295	4	0.062824			
Total	4.49652	8				

3.1 Grinding Wheel Rotational Speed Effect on Luminal Gain and MRR

Figure 3.2 shows the rotational speed effect on luminal gain and MRR. The standard deviation of each experiment was also presented in the figures as error bars.

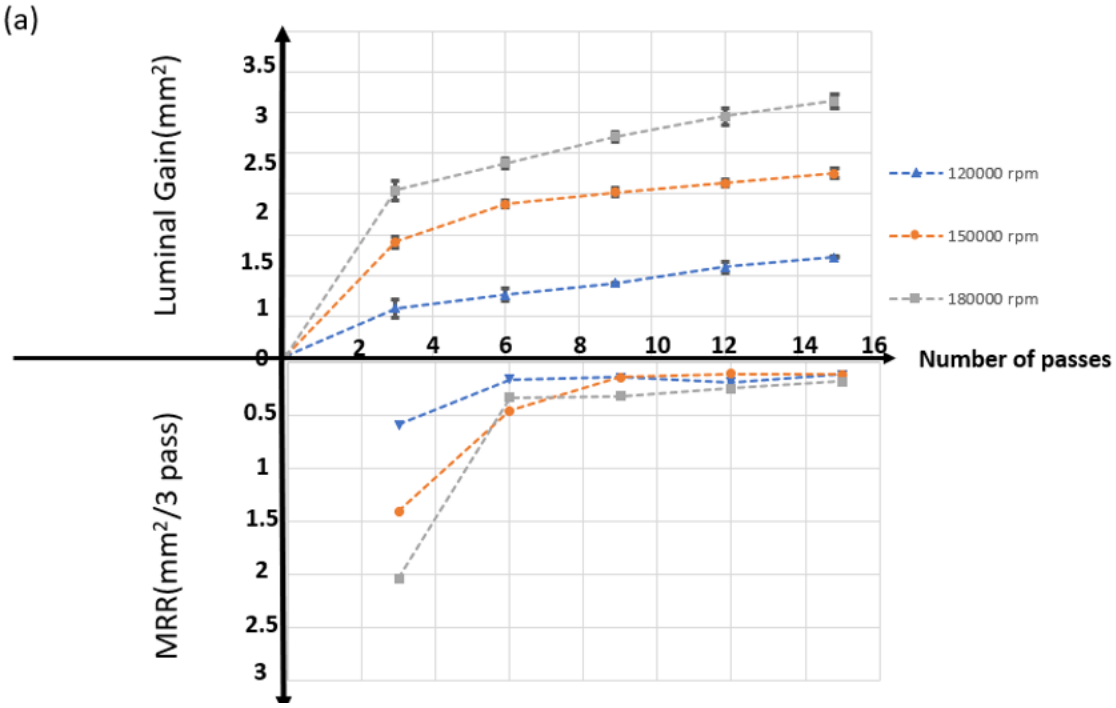

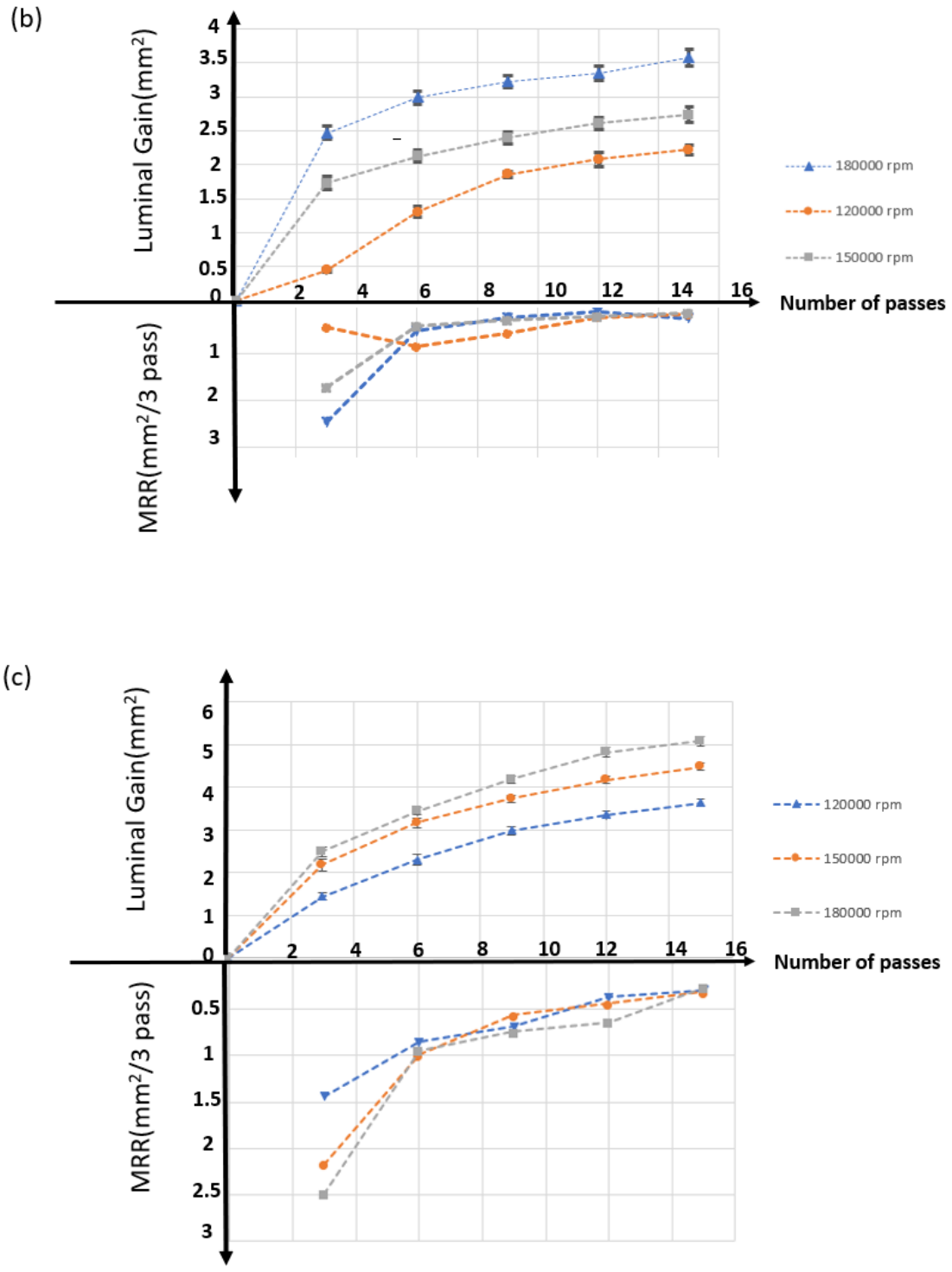

Figure 3.2 Luminal gain and MRR change with the increase of the grinding passes at three rotational speeds of 120,000, 150,000, and 180,000 rpm using the grinding wheel diameter of (a) 1.25, (b) 1.5, and (c) 1.75 mm.

For the same grinding wheel size, both luminal gain and RA MMR increase with the rotational speed. At the same grinding wheel size and the number of pass, the higher rotational speed leads to larger luminal gain and MRR. With the increase of the number of passes, the MRR decreases at any given grinding wheel rotational speed and size.

3.2 Grinding Wheel Size Effect on Luminal Gain and MRR

Figures 3.3 (a – c) show the grinding wheel size effect on luminal gain and MRR. The standard deviation of each experiment was also presented in the figures.

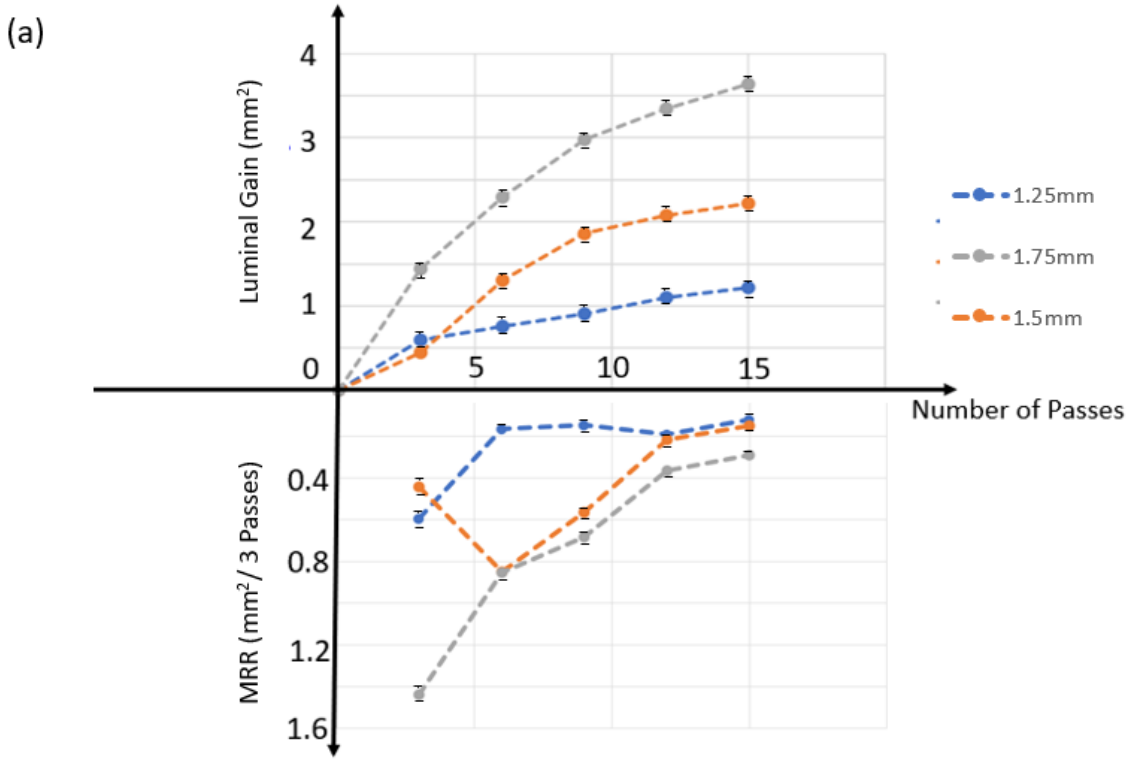

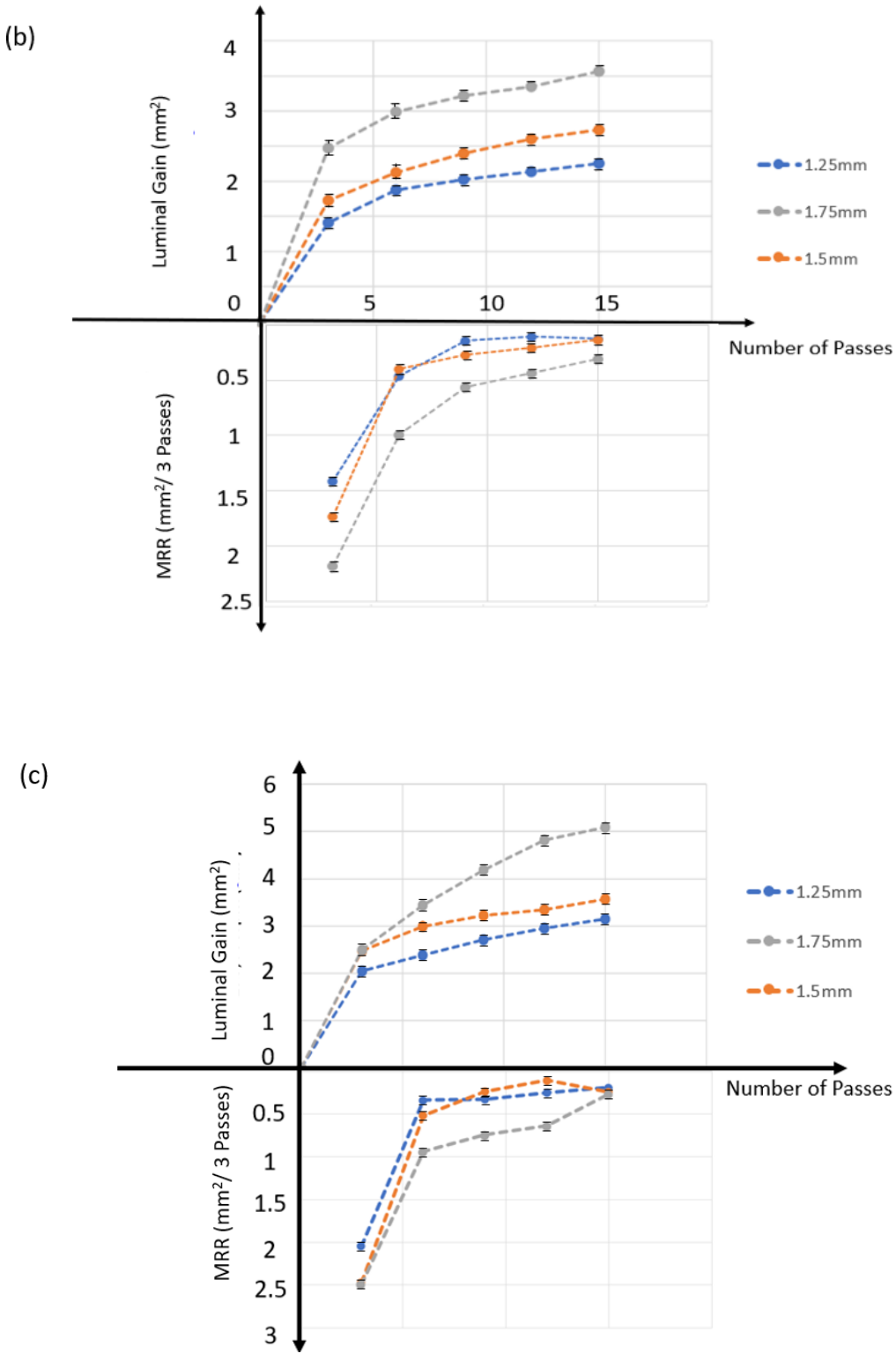

Figure 3.3 Luminal gain and MRR change with the increase of the grinding wheel sizes at three rotational speeds of 120,000, 150,000, and 180,000 rpm using the grinding wheel diameter of (a) 1.25, (b) 1.5, and (c) 1.75 mm.

As shown in Figure 3.3 (a – c), for the same rotational speed, both luminal gain and RA MMR increase with the increasing of the grinding wheel sizes. At the same rotational speed and pass value, the larger grinding wheel size corresponds to larger luminal gain and MRR. With the increase of the number of passes, the MRR decreases at any given grinding wheel rotational speed and size.

CHAPTER 4

DISCUSSION

In this discussion, an analytical model of RA MRR was derived based on the analogy between RA. Due to the lack of a thorough understanding of the RA grinding mechanism, the proposed model was not able to fully capture the experimental data. However, we hope this discussion could lead to a deeper understanding of the RA MRR and the model can be improved when more data available on RA grinding is in the future.

4.1 Analogy between RA and Constant Force Grinding

The grinding wheel motion of RA cannot be actively controlled due to the lack of stiffness in this RA system with the long, a flexible drive shaft was required to navigate through the tortuous arterial path. Most of the MRR models from the conventional grinding or machining with a fixed spindle of high stiffness, capable of achieving defined workpiece and grinding velocities and the depth of cut, are not applicable to RA. Instead, considering the grinding wheel orbital motion [32] induced centrifugal force, we find RA analogous to the constant force grinding processes, for example the belt grinding and hand polishing.

As shown in Figure 4.1, in belt grinding (Figure 4.1 (a)) and hand polishing (Figure 4.1 (b)) processes, the contact force, relatively constant, is controlled by the operator. This constant contact force between the workpiece and the grinding/polishing tool is a key factor affecting the MRR in these processes. Similarly, in RA (Figure 4.1 (c)), according to the grinding wheel motion study conducted by Zheng et al [32], the grinding wheel at a constant rotational frequency (Ω) within the blood flow in the artery will develop an orbital motion, looping around

the arterial lumen at a constant orbital frequency (ω), which will lead to a constant centrifugal force, F_c, on the grinding wheel supplied by the contact between the grinding wheel and the arterial wall. This centrifugal force in RA, comparable to the manual applied contact force in constant force grinding, determines the MRR with the grinding velocity.

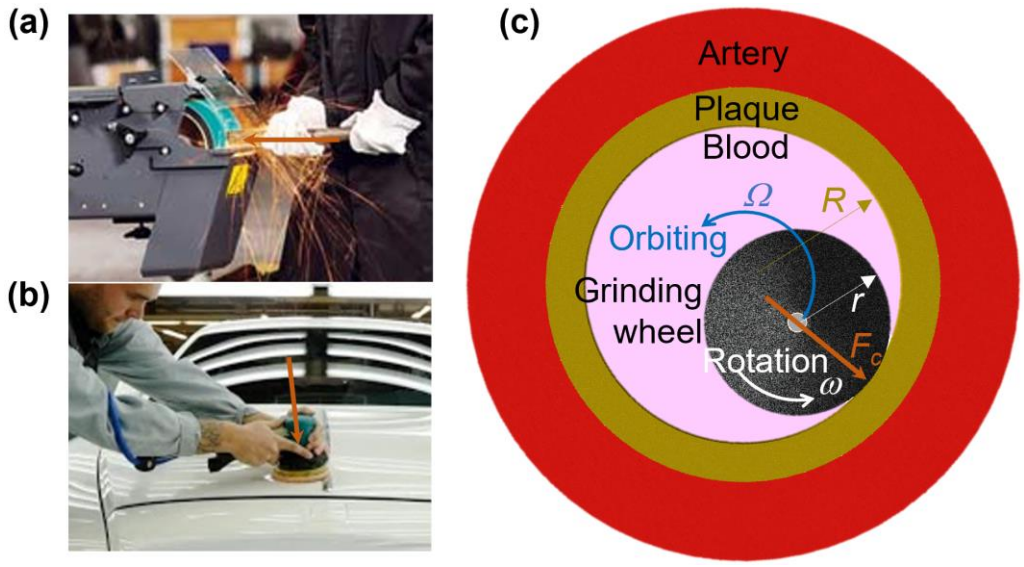

Figure 4.1: The analogy between constant force grinding and RA: (a) a constant force applied from the operator's hand to the workpiece-belt grinder contact, (b) a constant force applied in manual polishing, and (c) the orbital motion induced centrifugal force applied from the RA grinding wheel to the plaque for grinding. F_c is the centrifugal force generated by wheel orbital motion. R is the radius of the arterial lumen. r is the radius of the grinding wheel. Ω and ω are the grinding orbital and rotational frequency, respectively.

4.2 MRR Modeling in Constant Force Grinding

MRR models in constant force grinding, for example the belt grinding, have been developed. Hamann et al. proposed an analytical model [49]:

$$MRR = C_A K_t k_t \frac{V_b}{V_w L_w} F_A \quad (4.1)$$

where C_A is MRR grinding process constant, k_t is constant of resistance of the workpiece with grinding ability of the belt, belt wearing factor k_t, grinding rate V_b, feed-in rate V_w, machining width L_w. And normal force F_A.

Preston's [50] fundamental polishing equation is similar to Hamann's analytical model, which states that MRR of a grinding process is related to the relative velocity R_v and polishing pressure, P. The equation is shown as follows:

$$MRR = CPR_v \quad (4.2)$$

where C is a parameter determined by each polishing system. Both models indicate the velocity and the normal force are proportional to the relative grinding velocity and normal force.

4.3 RA MRR Model

Based on the aforementioned analogy between RA and the constant force grinding, as well as the analytical models developed for belt grinding, an analytical model for RA can be developed. The contact force in RA, as shown in Figure 4.1 (c), is the centrifugal force induced by the grinding wheel orbital motion, which can be described in the equation below:

$$F_c = m(R - r)\Omega^2 \quad (4.3)$$

where m is the mass of grinding wheel, R and r are the radius of the arterial lumen and the grinding wheel, respectively.

According to Zheng's study [51], the RA grinding wheel orbital frequency is proportional to its rotational frequency:

$$\Omega = a\omega \tag{4.4}$$

where a is a constant.

Substituting Ω in Equation 4.3 by Equation 4.4, the contact force can be calculated based on the grinding wheel rotational speed as:

$$F_c = m(R - r)a^2\omega^2 \tag{4.5}$$

As shown in Figure 4.1 (c), the grinding wheel rotational and orbital directions are the same. The relative velocity between the abrasives on the grinding wheel and artery wall V is the addition between the grinding wheel surface speed and the grinding wheel linear speed due to orbital motion, which can be calculated as:

$$V = \omega r + \Omega(R - r) \tag{4.6}$$

According to the MRR model in constant force grinding [61, 62] (Equation 4.2), with Equations 4.5 and 4.6 integrated, the RA MRR can be modeled as:

$$MRR = \ [r + a(R - r)](R - r)a^2\omega^3 m \tag{4.8}$$

To validate this model, we examined the MRR at the first grinding passes when R = 2 mm, the initial value is a constant across different grinding wheel rotational speeds and sizes. Figures 4.2 and 4.3 were plotted based on the data from experiment result, which is plotted and compared with formular (4.8) to see if they have the same trend.

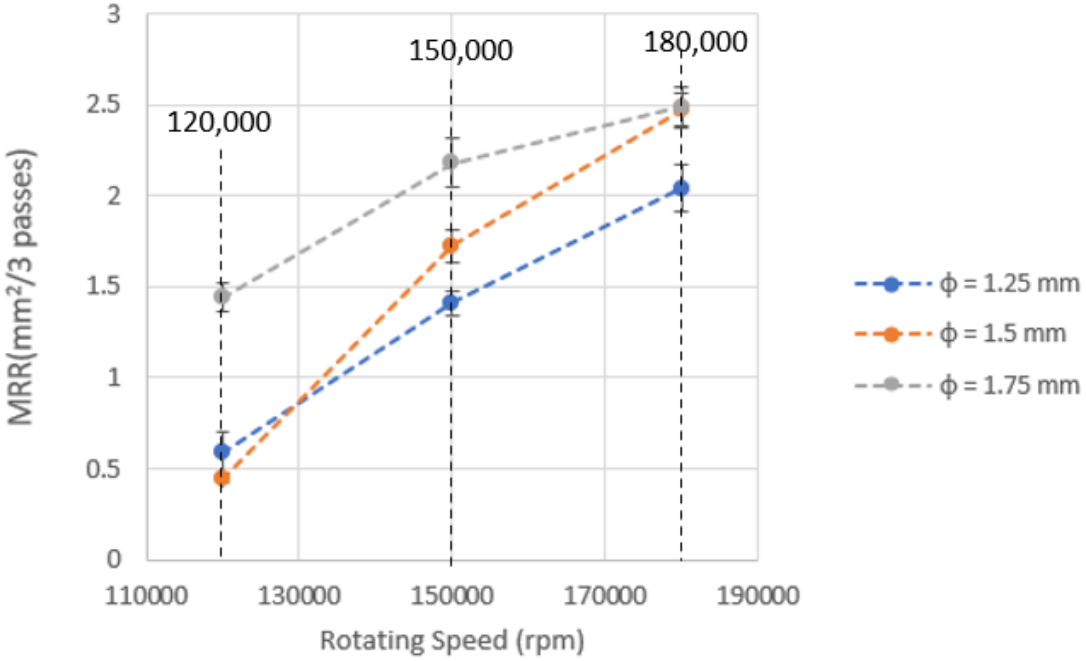

Figure 4.2: MRR for different grinding wheel at rotational speed of 120,000, 150,000 and 180,000 rpm.

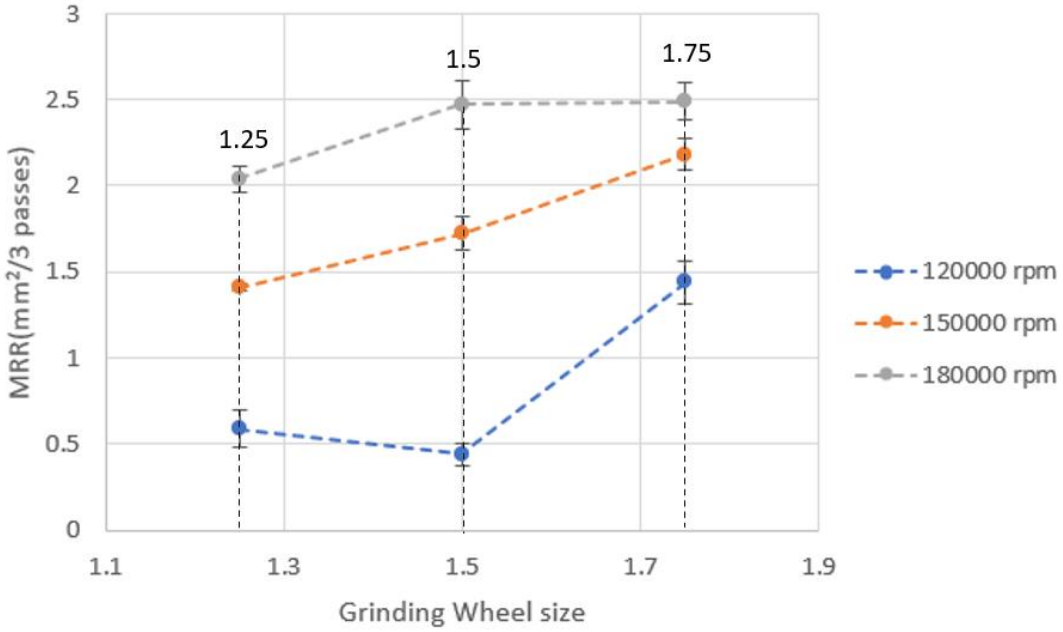

Figure 4.3: MRR at different rotational speeds for different grinding wheel sizes of ϕ1.25, ϕ1.5 and ϕ1.75 mm.

As can be observed in Figure 4.2, at a constant grinding wheel diameter, even though the MRR increases with the rotational speed, the rate of the MRR increase drops at the higher rotational speed. This cannot be explained by the model shown in Equation 4.8 where MRR is governed by the third order of the rotational speed. Similarly, at a constant grinding wheel rotational speed shown in Figure 4.3, the relationship between MRR and the wheel size is not well captured by Equation 4.8.

We realized that the analogy between RA and constant force grinding has limitations. During constant force grinding, the contact between the workpiece and the grinding tool is maintained throughout the process. However, during RA, due to the flexibility of the drive shaft, once the grinding wheel contacts the plaque material, the grinding forces will push the grinding wheel away from the arterial wall. It is the hydraulic force from the blood flow that drives

grinding wheel back in contact with the arterial wall. And again, the grinding wheel will be in contact with the arterial wall, generating grinding forces, and bounce away. This grinding wheel bouncing effect, also known as discontinuous grinding in RA, has been observed and introduced by Zheng et al [22]. Accordingly, besides contact force and relative velocity, in RA, the frequency of the grinding wheel bouncing on the arterial wall is the third factor affecting the MRR. This bouncing frequency is complicated by the grinding wheel rotational speed, grinding forces, and the hydrodynamic force from the blood flow and has not been well investigated. Without this bouncy frequency, the RA MRR model cannot be reliably developed.

Besides the lack of understanding in RA grinding wheel bouncing frequency, the luminal radius, R, is increasing with the number of grinding passes. To fully capture the RA MRR, a mathematical description of the luminal gain over time is required as well.

CHAPTER 5

CONCLUSIONS AND FUTURE STUDY

5.1 Conclusions

RA is an interventional procedure that utilizes a high-speed grinding wheel driven by a long, flexible shaft to pulverize calcified atherosclerotic plaque inside arteries, restore blood flow, and treat cardiovascular diseases. RA has been studied extensively from both clinical and engineering perspectives, but still challenged by high complication rates and confusions in operational guidelines. This thesis studied the MRR in the grinding of calcified plaque by RA. Experiment methods and procedures were developed to investigate the effects of the grinding wheel rotational speed and size on RA MRR. In this experiment, the calcified plaque surrogate and a tissue phantom were designed and built to simulate the diseased artery. Three rotational speeds (120,000, 150,000, and 180,000 rpm) and three grinding wheel diameters (1.25, 1.5, and 1.75 mm) were tested for MRR evaluation. The major achievements of this thesis include:

(1) Design and fabrication of the tissue phantom. A tissue phantom was designed to mimic the human artery. The material selection of the tissue phantom is the most challenging process in this study. Since the water was circulated through the whole system, the tissue phantom should be well sealed to prevent water leakage. The tissue phantom surface coating material should be flexible to simulate the surrounding healthy tissue and reduce the damage caused by the rotational abrasive wheel. Excessive grinding and material loss at the entrance of the tissue phantom would cause deviations of the simulated physiological boundary conditions, resulting in grinding wheel entrapment or unstable

motion. The rubber material used in our experiment can effectively prevent being worn out by the grinding wheel. Moreover, the geometric design of the tissue phantom makes it easier to exchange the samples compared to other tissue phantom structures from previous studies.

(2) Design and fabrication of calcified plaque surrogates. Previous studies have investigated the suitable surrogate that can mimic the human calcified plaque. Some studies used biological materials, but the modeling process is hard to replicate. The material selected in our study, Ultracal-30 plaster, is widely available with a mechanical property proven to be suitable for calcified plaque simulation. The procedure of calcified plaque surrogate fabrication using Ultracal-30 has been developed using soft silicone mold casting. Our proposed procedure can be readily adopted and adapted for different geometries for other studies and purposes.

(3) Engineering bench-top test setup for MRR quantification. The bench-top test setup developed in this study can capture key features of the physiological conditions for RA operation, including the atherosclerotic lesion, arterial path, and blood flow. RA operational guidelines can be individually controlled for engineering investigation. Comparing to animal, cadaveric, or human subject models, this proposed setup is more suitable for quantitative analysis.

(4) Quantification of the RA MRR. Together with the design of the calcified plaque surrogate and tissue phantom assembly, a microscopy and image processing-based approach was developed to quantify the RA MRR. Considering the small amount of material removed during RA, we believe this is an optimal method for RA MRR quantification.

The discoveries and key conclusions of this thesis are:

1) The luminal gain and MRR increase with the grinding wheel size at a given wheel rotational speed.
2) The luminal gain and MRR increase with the grinding wheel rotational speed when the same size grinding wheel is used.
3) During RA, at the same grinding wheel speed and size, the MRR decreases with the increase of the number of grinding passes.

These findings provide insights in the RA grinding mechanism and operation. These results are new to the clinical field, even though they might be intuitive to mechanical engineering and grinding society. The RA MRR was only investigated in two previous studies [37, 38] which were not able to reach any conclusive results.

The results in RA MRR observed in this study could lead to improvement of RA clinical guidelines and device design. In clinical practice, RA has time limits: each grinding process cannot exceed 30 s and the total operation time should not exceed five minutes [54]. Higher MRR can be beneficial to RA in terms of efficiency. However, to optimize RA clinical guidelines for optimal outcomes, besides MRR, the grinding wheel size and speed effects on grinding force, temperature, and debris size need to be considered.

5.2 Future Work

The methodologies and models proposed in this thesis could be further improved and extended in the following directions:

(1) With the method developed in this thesis, a wider range of grinding wheel rotational speed and size could be investigated to gain more data on RA MRR. Beyond RA, the MRR for other similar grinding-based atherectomy, including the orbital atherectomy, can be characterized.

(2) This study focused on two most important RA operational guidelines, grinding wheel rotational speed and wheel size. Other factors, including the grinding wheel translational speed and pattern can be further investigated, even though clinical guidelines in this regard have been relatively consistent.

(3) The bench-top test and tissue phantom design captured the main physiological conditions in RA operation but still were simplified with the straight artery and regular cylindrical lumen. Future studies can take the arterial curvature and irregular lumen surface morphology into consideration.

(4) In the discussion of this thesis, an analytical model of RA MRR was attempted by not validated by the experimental data due to missing information in RA grinding mechanism. With a more thorough understanding of the RA grinding wheel motion and force in the future, an improved analytical model based on constant force grinding can be developed to explain the RA MRR.

REFERENCE

[1] Sempos, Christopher T., Diane E. Bild, and Teri A. Manolio. "Overview of the Jackson Heart Study: a study of cardiovascular diseases in African American men and women." *The American journal of the medical sciences* 317, no. 3 (1999): 142-146.

[2] Jamison, Dean T., Joel G. Breman, Anthony R. Measham, George Alleyne, Mariam Claeson, David B. Evans, Prabhat Jha, Anne Mills, and Philip Musgrove, eds. "Disease control priorities in developing countries." (2006).

[3] Virani, Salim S., Alvaro Alonso, Hugo J. Aparicio, Emelia J. Benjamin, Marcio S. Bittencourt, Clifton W. Callaway, April P. Carson et al. "Heart disease and stroke statistics—2021 update: a report from the American Heart Association." *Circulation* 143, no. 8 (2021): e254-e743.

[4] Falk, Erling. "Pathogenesis of atherosclerosis." *Journal of the American College of cardiology* 47, no. 8S (2006): C7-C12.

[5] Wilens, S. L. "Cowdry's Arteriosclerosis: A Survey of the Problem." *JAMA* 201, no. 3 (1967): 211-211.

[6] Aziz, Maria, and K. S. Yadav. "Pathogenesis of atherosclerosis a review." *Med Clin Rev* 2, no. 3 (2016): 1-6.

[7] Willis, Monte, Jonathon W. Homeister, and James R. Stone, eds. *Cellular and molecular pathobiology of cardiovascular disease*. Academic Press, 2013.

[8] Bergheanu, S. C., M. C. Bodde, and J. W. Jukema. "Pathophysiology and treatment of atherosclerosis." *Netherlands Heart Journal* 25, no. 4 (2017): 231-242.

[9] "Atherosclerosis: symptoms and treatments". Harvard Health Publishing, December 10, 2014. © 2021 by The President and Fellows of Harvard College

[10] Cockburn, James, Tiffany Kemp, Peter Ludman, Tim Kinnaird, Tom Johnson, Nick Curzen, Derek Robinson et al. "Percutaneous coronary intervention in octogenarians: A risk scoring system to predict 30‐day outcomes in the elderly." *Catheterization and Cardiovascular Interventions* (2020).

[11] "Procedure Information Sheet-Percutaneous Coronary Intervention (PCI)". HONG KONG Gleneagles. GCVL-F34-R1-02/18.

[12] Marra, Steven P., Charles P. Daghlian, Mark F. Fillinger, and Francis E. Kennedy. "Elemental composition, morphology and mechanical properties of calcified deposits obtained from abdominal aortic aneurysms." *Acta biomaterialia* 2, no. 5 (2006): 515-520.

[13] Güneş, Yılmaz, İsa Sincer, and Emrah Erdal. "Catheter-directed intra-arterial thrombolysis for lower extremity arterial occlusions." *Anatolian journal of cardiology* 22, no. 2 (2019): 54.

[14] Tomey, Matthew I., Annapoorna S. Kini, and Samin K. Sharma. "Current status of rotational atherectomy." *JACC: Cardiovascular Interventions* 7, no. 4 (2014): 345-353.

[15] Chen, Chun-Chi, and I-Chang Hsieh. "Application of rotational atherectomy in the drug-eluting stent era." *Journal of geriatric cardiology: JGC* 10, no. 3 (2013): 213.

[16] Sharma, Samin K., Matthew I. Tomey, Paul S. Teirstein, Annapoorna S. Kini, Arthur B. Reitman, Arthur C. Lee, Philippe Généreux et al. "North American expert review of rotational atherectomy." *Circulation: Cardiovascular Interventions* 12, no. 5 (2019): e007448.

[17] Whitlow, Patrick L., Theodore A. Bass, Robert M. Kipperman, Barry L. Sharaf, Kalon KL Ho, Donald E. Cutlip, Yan Zhang et al. "Results of the study to determine rotablator and transluminal angioplasty strategy (STRATAS)." *The American journal of cardiology* 87, no. 6 (2001): 699-705.

[19] Safian, Robert D., Ted Feldman, David WM Muller, Denise Mason, Theodore Schreiber, Bruce Haik, Michael Mooney, and William W. O'Neill. "Coronary angioplasty and Rotablator atherectomy trial (CARAT): immediate and late results of a prospective multicenter randomized trial." *Catheterization and cardiovascular interventions* 53, no. 2 (2001): 213-220.

[20] Barbato, Emanuele, Didier Carrié, Petros Dardas, Jean Fajadet, Georg Gaul, Michael Haude, Ahmed Khashaba et al. "European expert consensus on rotational atherectomy." *EuroIntervention: journal of EuroPCR in collaboration with the Working Group on Interventional Cardiology of the European Society of Cardiology* 11, no. 1 (2015): 30-36.

[21] Mota, Paula, Adam de Belder, and António Leitão-Marques. "Rotational atherectomy: Technical update." *Revista Portuguesa de Cardiologia (English Edition)* 34, no. 4 (2015): 271-278.

[22] Zheng, Yihao. "Grinding wheel motion and force analysis in atherosclerotic plaque removal by Atherectomy." PhD diss., 2016.

[23] Zheng, Yihao, Yang Liu, Yao Liu, and Albert J. Shih. "Experimental investigation of the grinding force in rotational atherectomy." *Procedia Manufacturing* 5 (2016): 838-848.

[24] Shih, Albert J., Yao Liu, and Yihao Zheng. "Grinding wheel motion, force, temperature, and material removal in rotational atherectomy of calcified plaque." *CIRP Annals* 65, no. 1 (2016): 345-348.

[25] Zheng, Yihao, Barry Belmont, and Albert J. Shih. "Experimental investigation of the grinding wheel dynamics in atherectomy." *Procedia Manufacturing* 1 (2015): 879-891.

[26] Liu, Yao, Yang Liu, Yihao Zheng, Beizhi Li, and Albert Shih. "Catheter thermal energy generation and temperature in rotational atherectomy." *Medical engineering & physics* 70 (2019): 29-38.

[27] Reisman, Mark, Brandon J. Shuman, Dave Dillard, Ruigao Fei, Kenneth H. Misser, Lucas S. Gordon, and Verna Harms. "Analysis of low-speed rotational atherectomy for the reduction of platelet aggregation." *Catheterization and cardiovascular diagnosis* 45, no. 2 (1998): 208-214.

[28] Liu, Yao, Beizhi Li, Lingfei Kong, Yang Liu, and Yihao Zheng. "Experimental and modeling study of temperature in calcified plaque grinding." *The International Journal of Advanced Manufacturing Technology* 99, no. 1 (2018): 1013-1021.

[29] Liu, Yao, Beizhi Li, Yihao Zheng, and Albert Shih. "Experiment and smooth particle hydrodynamics simulation of debris size in grinding of calcified plaque in atherectomy." *CIRP Annals* 66, no. 1 (2017): 325-328.

[30] Zheng, Yihao, Jingxuan Lyu, Yang Liu, Jason Lo, Ata Susamaz, Hitinder S. Gurm, and Albert J. Shih. "Grinding Wheel Motion and Force During Plaque Removal by Rotational Atherectomy in Angulated Coronary Artery." In *International Manufacturing Science and Engineering Conference*, vol. 51357, p. V001T05A010. American Society of Mechanical Engineers, 2018.

[31] Zheng, Yihao, Yang Liu, John J. Pitre, Joseph L. Bull, Hitinder S. Gurm, and Albert J. Shih. "Computational fluid dynamics modeling of the burr orbital motion in rotational atherectomy with particle image velocimetry validation." *Annals of biomedical engineering* 46, no. 4 (2018): 567-578.

[32] Zheng, Yihao, Barry Belmont, and Albert J. Shih. "Experimental investigation of the abrasive crown dynamics in orbital atherectomy." *Medical engineering & physics* 38, no. 7 (2016): 639-647.

[33] Lyu, Jessie Jingxuan, Xiang Wu, Yao Liu, Yang Liu, Annie Dian-Ru Li, Yihao Zheng, and Albert Shih. "A miniature nickel-diamond electroplated wheel for grinding of the arterial calcified plaque." *Procedia Manufacturing* 34 (2019): 222-227.

[34] Kim, Min-Hyeng, Hyung-Jung Kim, Nicholas N. Kim, Hae-Sung Yoon, and Sung-Hoon Ahn. "A rotational ablation tool for calcified atherosclerotic plaque removal." *Biomedical microdevices* 13, no. 6 (2011): 963-971.

[35] Nakao, M., K. Tsuchiya, W. Maeda, and D. Iijima. "A rotating cutting tool to remove hard cemented deposits in heart blood vessels without damaging soft vessel walls." *CIRP annals* 54, no. 1 (2005): 37-40.

[36] Zheng, Yihao, Yao Liu, Yang Liu, and Albert J. Shih. "Multigrain Smoothed Particle Hydrodynamics and Hertzian Contact Modeling of the Grinding Force in Atherectomy." *Journal of Manufacturing Science and Engineering* 141, no. 4 (2019).

[37] Kobayashi, Norihiro, Masahiro Yamawaki, Keisuke Hirano, Motoharu Araki, Tsuyoshi Sakai, Yasunari Sakamoto, Shinsuke Mori et al. "Additional debulking efficacy of low-speed rotational atherectomy after high-speed rotational atherectomy for calcified coronary lesion." *The International Journal of Cardiovascular Imaging* 36, no. 10 (2020): 1811-1819.

[38] Yamamoto, Takanobu, Sawako Yada, Yuji Matsuda, Hirofumi Otani, Shunji Yoshikawa, Taro Sasaoka, Yu Hatano et al. "A novel rotablator technique (low-speed following high-speed rotational atherectomy) can achieve larger lumen gain: evaluation using optimal frequency domain imaging." *Journal of interventional cardiology* 2019 (2019).

[39] Rahdert, David A., William L. Sweet, Fermin O. Tio, Christian Janicki, and Dennis M. Duggan. "Measurement of density and calcium in human atherosclerotic plaque and implications for arterial brachytherapy." *Cardiovascular Radiation Medicine* 1, no. 4 (1999): 358-367.

[40] Tzafriri, Abraham R., Fernando Garcia-Polite, Brett Zani, James Stanley, Benny Muraj, Jennifer Knutson, Robert Kohler, Peter Markham, Alexander Nikanorov, and Elazer R. Edelman. "Calcified plaque modification alters local drug delivery in the treatment of peripheral atherosclerosis." *Journal of Controlled Release* 264 (2017): 203-210.

[41] Chisena, Robert S., Jordan Sengenberger, Albert J. Shih, and Hitinder Gurm. "Novel preclinical method for evaluating the efficacy of a percutaneous treatment in human ex vivo calcified plaque." *Medical & Biological Engineering & Computing* 59, no. 4 (2021): 799-811.

[42] Kawase, Yoshiaki, Naritatsu Saito, Shin Watanabe, Bingyuan Bao, Erika Yamamoto, Hiroki Watanabe, Hirooki Higami, Hitoshi Matsuo, Katsumi Ueno, and Takeshi Kimura. "Utility of a scoring balloon for a severely calcified lesion: bench test and finite element analysis." *Cardiovascular intervention and therapeutics* 29, no. 2 (2014): 134-139.

[43] Reisman, Mark, Brandon J. Shuman, and Verna Harms. "Analysis of heat generation during rotational atherectomy using different operational techniques." *Catheterization and cardiovascular diagnosis* 44, no. 4 (1998): 453-455.

[44] Calcified Plaque Models (bonesim.com). CALCIFIED PLAQUE LESION MODELS (CPLS). (574) 551-9814 support@bonesim.com.

[45] Song, Xiaoyang, Taiji Adachi, Yoshiaki Kawase, Takeshi Kimura, and Naritatsu Saito. "Efficacy of the Wolverine cutting balloon on a circumferential calcified coronary lesion: Bench test using a three-dimensional printer and computer simulation with the finite element method." *Cardiovascular Intervention and Therapeutics* (2021): 1-11.

[46] Kawase, Yoshiaki, Naritatsu Saito, Shin Watanabe, Bingyuan Bao, Erika Yamamoto, Hiroki Watanabe, Hirooki Higami, Hitoshi Matsuo, Katsumi Ueno, and Takeshi Kimura. "Utility of a scoring balloon for a severely calcified lesion: bench test and finite element analysis." *Cardiovascular intervention and therapeutics* 29, no. 2 (2014): 134-139.

[47] Scott, Holly A., Andrew Archuleta, and Robert Splinter. "Calcified lesion modeling for excimer laser ablation." In *Photonics North 2009*, vol. 7386, p. 738608. International Society for Optics and Photonics, 2009.

[48] Chisena, Robert S., Jordan Sengenberger, Albert J. Shih, and Hitinder Gurm. "Novel preclinical method for evaluating the efficacy of a percutaneous treatment in human ex vivo calcified plaque." *Medical & Biological Engineering & Computing* 59, no. 4 (2021): 799-811.

[49] Hammann, Gerhard. *Modellierung des Abtragsverhaltens elastischer, robotergeführter Schleifwerkzeuge*. Vol. 123. Springer-Verlag, 2013.

[50] Preston, F. W. "The theory and design of plate glass polishing machines." *Journal of Glass Technology* 11, no. 44 (1927): 214-256.

[51] Sakakura, Kenichi, Taku Inohara, Shun Kohsaka, Tetsuya Amano, Shiro Uemura, Hideki Ishii, Kazushige Kadota et al. "Incidence and determinants of complications in rotational atherectomy: insights from the National Clinical Data (J-PCI Registry)." *Circulation: Cardiovascular Interventions* 9, no. 11 (2016): e004278.

[52] García-Herrera, Claudio M., José M. Atienza, F. J. Rojo, Els Claes, G. V. Guinea, Diego J. Celentano, Carlos Garcia-Montero, and Raúl L. Burgos. "Mechanical behaviour and rupture of normal and pathological human ascending aortic wall." *Medical & biological engineering & computing* 50, no. 6 (2012): 559-566.

[53] Claes, E., J. M. Atienza, G. V. Guinea, F. J. Rojo, J. M. Bernal, J. M. Revuelta, and M. Elices. "Mechanical properties of human coronary arteries." In *2010 Annual International Conference of the IEEE Engineering in Medicine and Biology*, pp. 3792-3795. IEEE, 2010.

[54] Rotablator, *reference from guidelines*. Boston scientific.